Nano Research

Open Access

Research Article

Cactus-inspired freeze-printed SiO_2/ZrO_2 aerogels with programmable configuration for extreme thermal insulation

Huikang Li[1], Weilin Liao[1], Bingcheng Li[1], Xiaosen Su[1], Ke Zhang[2], Fei Fang[1] ✉, and Xudong Huang[2] ✉

[1] *Department of Engineering Mechanics, Tsinghua University, Beijing 100084, China*
[2] *Department of Aeronautics & Astronautics Engineering, Tsinghua University, Beijing 100084, China*

Cite this article: *Nano Research*, **2026**, *19*, 94908587. https://doi.org/10.26599/NR.2026.94908587

ABSTRACT: Aerogels have attracted extensive attention due to their remarkable properties, such as lightweight and low thermal conductivity. However, it remains challenging to simultaneously achieve high temperature insulation (> 1000 °C) and improve mechanical performance. Herein, we report a cactus-inspired spiral structure preparation strategy via freezing-assisted direct ink writing (DIW). By synergistically controlling the rotation angle (θ) and printing spacing (x), we fabricate SiO_2/ZrO_2 aerogels with programmable macroscopic spiral architectures. The SiO_2/ZrO_2 aerogels with θ = 40° and x = 1.3 mm exhibit excellent thermal insulation (30.2 $mW \cdot m^{-1} \cdot K^{-1}$). However, the compressive strength is only 159.3 kPa at 24.2% fracture strain. To enhance the mechanical performance without compromising thermal insulation, an arctangent-topological DIW strategy is proposed, which employs the arctangent function α_n = arctan(1/n) to fabricate aerogels with four-fold rotational symmetry. When α_n = 26.6° (n = 2), the SiO_2/ZrO_2 aerogels exhibit a favorable thermal insulation performance (33.9 $mW \cdot m^{-1} \cdot K^{-1}$) while achieving a significant enhancement in compressive strength (341.7 kPa at 24.6% fracture strain). Application of SiO_2/ZrO_2 aerogels for thermal insulation of electronic chips and flame nozzles are demonstrated. The results demonstrate the feasibility of the SiO_2/ZrO_2 aerogels for high temperature applications. This study offers a strategy for developing of high-temperature aerogels with combined good thermal insulation and mechanical properties.

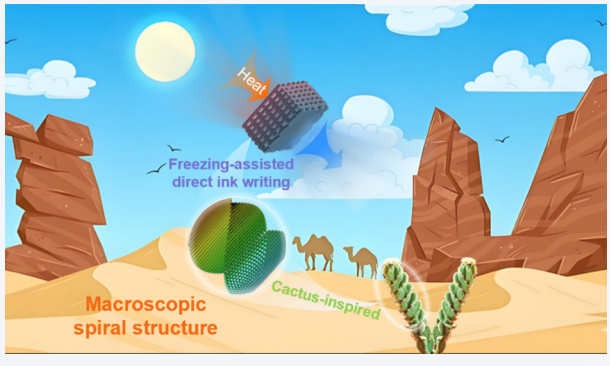

KEYWORDS: three-dimensional (3D) printing, direct ink writing, biomimetic design, silica aerogels, thermal insulation

1 Introduction

High-temperature protective materials are increasingly demanded for thermal management of electronics in extreme environment, as well as thermal insulation for engine nozzles in aerospace engineering, etc [1–3]. As high-performance lightweight thermal insulating materials, aerogels have attracted extensive attention [4].

Aerogels can be primarily categorized into organic and inorganic ones. Organic aerogels exhibit superior flexibility but suffer from limited thermal stability. Currently, polyimide (PI) aerogels demonstrate the highest heat resistance among organic aerogels, with a maximum service temperature of approximately 400 °C [5, 6]. Compared to organic aerogels, inorganic aerogels, predominantly SiO_2 and its composite, exhibit better high-temperature resistance, usually above 1000 °C, but are rather fragile. Zhang et al [7]. fabricated a SiO_2 composite aerogel using Al_2O_3 nanorods as a reinforcement phase. This aerogel with a thickness of 2 cm exhibited a surface temperature of 465 °C at a flame temperature of 1500 °C. But the fracture strain is only 2% at a compressive strength of 1.5 MPa [7]. Aerogels combining organic and inorganic phases have been explored to address the brittleness issue. Wang et al. [8] prepared a PI/SiO_2 composite aerogel, which achieved a strain of 80% under a compressive stress of 1.58 MPa. However, the presence of the organic phase limits its high temperature application, usually below 700 °C. Aerogels with good thermal insulation around 1000 °C, combined with mechanical excellence remains challenging.

Thermal insulation organisms existing in nature and through prolonged evolution may offer inspiration for the design of the aerogel structures [9–12]. Taking the cactus as an example, it thrives in hot and windy deserts. Its macroscopic spiral ridges extend the heat conduction path through multi-interface reflection and scattering, protecting internal tissues from high-temperature

Received: December 12, 2025; **Revised:** February 4, 2026
Accepted: February 19, 2026

✉Address correspondence to Fei Fang, fangf@mail.tsinghua.edu.cn; Xudong Huang, xdhuang@mail.tsinghua.edu.cn

damage. Simultaneously, the spiral ridges also help the cactus resist strong winds. Previous studies on spiral structures have already demonstrated their unique advantages in thermal insulation. Wang et al. [3] fabricated a ceramic aerogel with a spiral architecture by alternately stacking nanofibers and microfibers. At a flame temperature of 1200 °C, the surface temperature of the 15 mm-thick aerogel was only 134.7 °C [3]. Moreover, spiral structures also exhibit unique mechanical advantages. Zheng et al. [13] designed an Archimedean spiral structure to alleviate stress concentration, increasing the tensile strength of aerogel yarn from about 9.5 to 16.3 MPa. Zhang et al. [14] employed a graded spiral structure to induce stress decomposition, interlayer bridging and deformation energy dissipation, thereby toughening the aerogel. Wen et al. [15] designed a graded double-helix structure to guide crack deflection, contributing to the development of ultra-strong impact-resistant materials.

Direct ink writing (DIW), as an additive manufacturing technique, offers unique advantages in printing designed geometries and structures, compared with traditional aerogel-preparation methods [16–20]. When employing DIW for aerogel fabrication, optimization of the printing design is essential [21, 22]. Cui et al. [23] combined controllably shrinkable polyacrylic acid hydrogel with DIW, significantly increasing the mechanical strength of the aerogel from 0.5 MPa to approximately 15 MPa. Cheng et al. [24] adopted a suspended printing strategy, increasing the printing speed of aerogels to 167 mm·s^{-1} and substantially improving production efficiency. However, printed aerogels typically exhibit noticeable through-pores on the surface, which adversely affect their thermal insulation performance [25–28]. This phenomenon is closely related to the structural parameters during the aerogel printing process [29].

In this work, inspired by the unique spiral ridges structure of cactus, we combine freezing-assisted DIW with freeze-drying to obtain aerogels with high temperature resistance and mechanical flexibility. Through precise regulation of ink properties, we successfully fabricate SiO_2/ZrO_2 aerogels with controllable macroscopic structures and extreme thermal insulation performance. Matrix of SiO_2 aerogel is selected since its preparation from the tetraethyl orthosilicate (TEOS) precursor is quite reproducible. Addition of nanoparticles of ZrO_2 into the TEOS precursor is supposed to reinforce the lightweight of the SiO_2 matrix, and more importantly, to make the precursor solution ink-printable. Different content of ZrO_2 nanoparticles (0 wt.%, 10 wt.%, and 20 wt. %) was tested for DIW. By adjusting the rotation angle (θ) and printing spacing (x), SiO_2/ZrO_2 aerogels with tunable geometric configurations are prepared. Furthermore, an arctangent-topological DIW strategy is designed by employing the function α_n = arctan(1/n) to fabricate SiO_2/ZrO_2 aerogels with four-fold rotational symmetry, aiming to synergistically enhancing both thermal insulation and mechanical properties. Aerogels fabricated via these two printing strategies are subjected to thermal insulation tests under high-temperature flames at 600, 800, and 1000 °C, as well as uniaxial compression stress-strain tests. Finite element simulations using COMSOL Multiphysics are conducted to investigate the thermal insulation and compressive mechanical behaviors of SiO_2/ZrO_2 aerogels. Finally, the application of SiO_2/ZrO_2 aerogels for thermal insulation of electronic chips and flame nozzles are demonstrated. This work provides a feasible strategy for the structural design of aerogels with excellent high-temperature insulation and mechanical properties.

2 Experimental

2.1 Materials and ink preparation

The precursor ink primarily consists of four components: PVA (polyvinyl alcohol), TEOS ($Si(OC_2H_5)_4$), mullite microfibers (with a diameter of 100–200 nm and a length of 2–5 μm), and ZrO_2 (particle size of 30 nm) aqueous solution (15 wt.%). To prepare the ink, PVA powder (4 g) was added to deionized water (DI water, 36 mL) and stirred thoroughly for 2.5 h at 60 °C using a water bath. Subsequently, TEOS (25 mL) was added to DI water (22.5 mL) along with oxalic acid (0.112 g) as a catalyst and stirred thoroughly for 2.5 h at 60 °C in a water bath to obtain the TEOS hydrolysate. Following this, PVA solution (15 mL) and TEOS hydrolysate (30 mL) were combined with mullite microfibers (0.273 g) and stirred for 2 h at room temperature to ensure thorough mixing. Then, ZrO_2 aqueous solution (5 mL) was added, and the mixture was immediately subjected to ultrasonic vibration for 20 min at room temperature using an ultrasonic homogenizer (10% power output). The uniformly dispersed solution was then sealed and heat-treated in a 60 °C water bath for approximately 7 min to increase its viscosity, thereby achieving suitable printability.

2.2 Printing process and fabrication of SiO_2/ZrO_2 aerogels

The prepared ink was printed using a freezing-assisted DIW device employing a linear infill pattern, with fill border dimensions of 27 mm × 27 mm, 28 layers, a layer height of 0.45 mm, a nozzle diameter of 0.84 mm and a syringe barrel volume of 10 ml. Printing parameters included a pre-infusion time of 1 ms, pre-retraction distance of 0.1 mm, printing pressure of 0.09–0.11 Pa, printing speed of 12 mm·s^{-1}, print path spacing ranging from 1.3 to 1.8 mm, and print angle adjusted as needed. The cold-water tank temperature was set to 5 °C, while the low-temperature freezing platform was maintained at −25 °C. The printed aerogel structures were first pre-frozen at −79 °C for 2 h to ensure complete internal freezing, then subjected to freeze-drying for 18 h to sublimate the internal ice crystals. The freeze-dried aerogels underwent the following heating processes: heating from room temperature to 300 °C at 10 °C·min^{-1}, maintaining at 300 °C for 2 h, heating from 300 to 600 °C at 10 °C·min^{-1}, maintaining at 600 °C for 2 h, and finally passively cooling to room temperature, yielding the final SiO_2/ZrO_2 aerogels.

2.3 Characterization

Morphologies of the SiO_2/ZrO_2 aerogels were observed by a scanning electron microscope (Merin, Carl Zeiss AG, Germany) at an acceleration voltage of 5 kV, after being coated with gold. The thermal conductivity of the four distinct aerogel models was measured at room temperature using a hot disk TPS 3500 instrument (Hot Disk AB, Sweden). The aerogel samples (23 mm × 23 mm × 12 mm) were secured onto an iron stand, one side was subjected to intense heating using a high-temperature blowtorch (Beiyue 220, China), while thermal images of the opposite side were captured over a temperature range of 25 to 1200 °C using an infrared camera (Ti400, Fluke Corp., USA). The mechanical properties of the four different aerogel models, with approximate dimensions of 23 mm × 23 mm × 12 mm, were tested under uniaxial compression mode on an electronic universal testing machine (EZ-LX HS, Shimadzu Corp., Japan), employing a 1000 N load cell at a crosshead speed of 2 mm·min^{-1}. Rheological data were

measured and recorded using a rotational rheometer (Anton Paar Physica MCR 301/302, Austria) equipped with a 20 mm parallel-plate geometry and a set gap of 1 mm, with a torque range of 0.002 μNm to 200 mNm and a normal force range of 0.01 to 50 N. Specifically, the viscosity of the ink was determined under shear rate sweep conditions ranging from 0.01 to 100 s^{-1}. Thermal stability was assessed via thermogravimetric analysis (TGA, Pyris 1 TGA, PerkinElmer), with mass loss recorded under a nitrogen atmosphere at a heating rate of 16 °C·min^{-1}.

3 Results and discussion

3.1 Structural design of SiO_2/ZrO_2 aerogels

Figure 1(a) shows a cactus species, characterized by unique structure of spiral ridges. These spirally arranged ridges form multi-angular reflective surfaces that scatter incident light in various directions, thereby reducing the efficiency of light-to-heat conversion. In addition to minimizing the effective heat-receiving area, the alternating protrusions and grooves provide shading effects. The grooved regions also trap stagnant air, forming a natural insulating air layer. Rotation angles are quantified using θ and ϕ, where θ denotes the relative rotation between two adjacent layers, and ϕ defines the rotation of the current layer relative to the bottommost layer. It is noteworthy that the rotation angle θ varies significantly across different environments. Under extreme conditions such as intense light and high temperatures, the θ tends to be around 40°. In such settings, the cactus develops more ridges and denser spines to maximize thermal insulation. Conversely, in persistently windy environments, cactus exhibit smaller rotation angles (20° or even less) to enhance wind resistance and structural stability. Thus, the spiral ridges of cactus represent a biological adaptation that combines excellent thermal insulation with mechanical strength. DIW of this unique spiral configuration offers

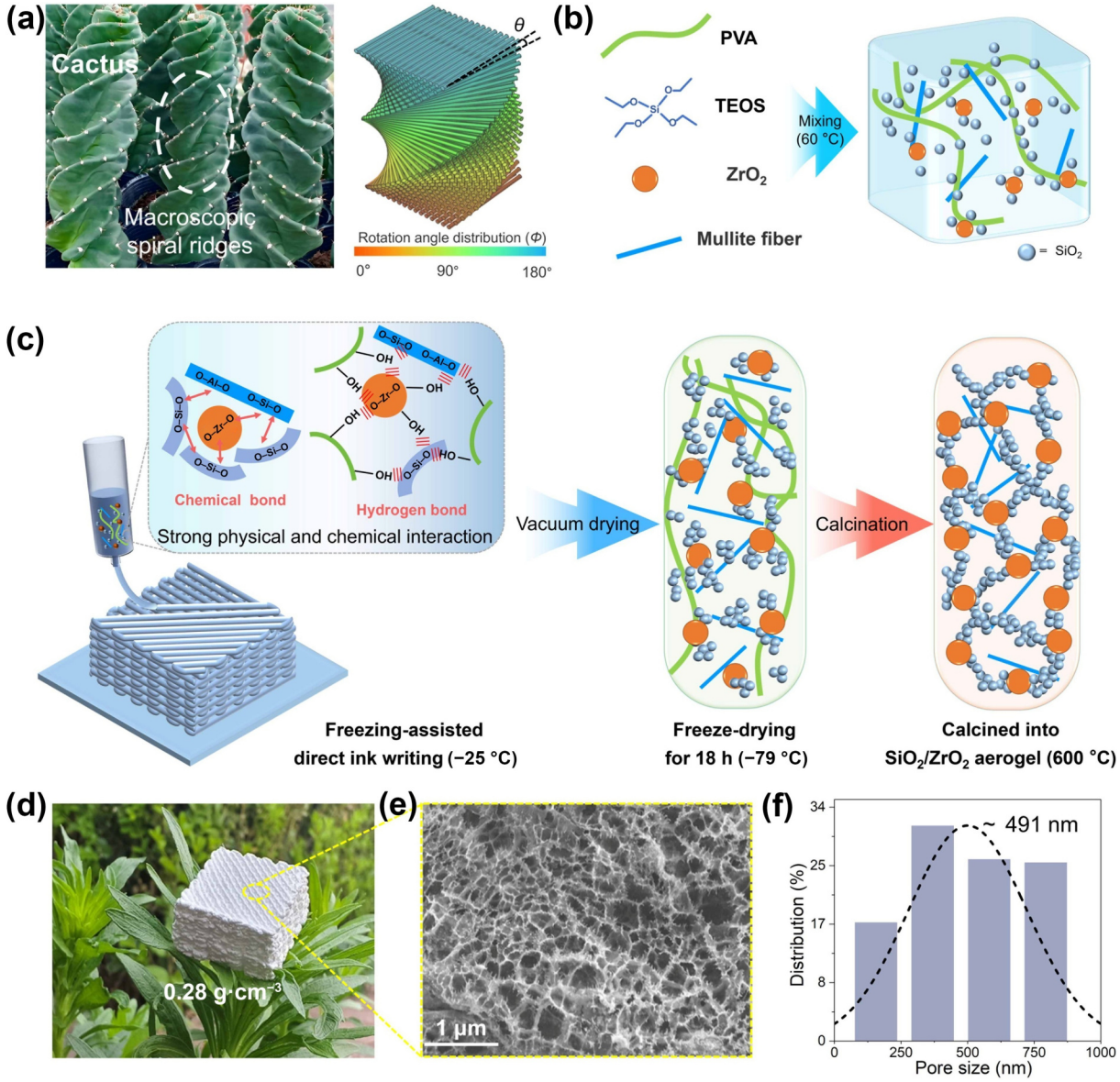

Figure 1 Structural design of SiO_2/ZrO_2 aerogels. (a) Spiral ridges of cactus. (b) Preparation of the precursor ink. (c) SiO_2/ZrO_2 aerogels are fabricated by freezing-assisted DIW, freeze-drying and calcination. (d)–(f) Low-density SiO_2/ZrO_2 aerogel (printing spacing x = 1.3 mm and rotation angle θ = 40°) with its SEM micrographs and internal pore distribution.

a promising approach to improve both thermal insulation and mechanical performance of the aerogels.

Figure 1(b) illustrates the preparation process of the ink. A 10 wt.% aqueous solution of PVA is mixed with a 49.9 wt.% TEOS hydrolysate at a volume ratio of 1:2 under stirring. Subsequently, a 20 wt.% aqueous suspension of ZrO_2 nanoparticles and 0.1 wt.% mullite ($3Al_2O_3{\cdot}2SiO_2$) microfibers are added. The mixture is then subjected to ultrasonication to achieve homogeneous dispersion, resulting in the precursor ink. As shown in Fig. 1(c), strong chemical bonds of Si–O–Si, Si–O–Zr, and Si–O–Al are formed in the solution of the mullite microfibers, ZrO_2 nanoparticles and TEOS. These bonds facilitate the effective embedding of ZrO_2 nanoparticles and mullite fibers into the siloxane network, thereby enhancing the overall strength of the system. Furthermore, due to the abundant hydroxyl groups, extensive hydrogen bonding interactions occurs among PVA, mullite microfibers, ZrO_2 nanoparticles, and TEOS in the ink. These hydrogen bonds play a critical role during printing. They contribute to higher ink viscosity prior to extrusion. Under strong shear forces during printing, the hydrogen bonds break, resulting in shear-thinning behavior and successful extrusion. After deposition, the hydrogen bonds rapidly reform to maintain gel morphology.

During the freezing-assisted direct ink writing process, as shown in Fig. 1(c), the temperature of the printing platform is maintained at −25 °C to rapidly solidify the ink. After printing, the gel is immediately frozen in a cold trap at −79 °C for 30 min. Subsequently, freeze-drying is performed to sublimate and remove the ice crystals formed during freezing. Finally, the freeze-dried SiO_2/ZrO_2 aerogels are subjected to calcination at 600 °C to remove the PVA. The crystalline structure of SiO_2/ZrO_2 aerogels remains while nanoporous pores are formed. Figure 1(d) demonstrates the lightweight nature of the SiO_2/ZrO_2 aerogels, with a measured density of 0.28 g·cm^{-3}.

3.2 Control of ink viscosity and printing parameters

The viscosity of the ink directly influences the morphology of the printed gel, making its regulation a critical step prior to printing. Firstly, the addition of ZrO_2 nanoparticles at varying mass fractions significantly affects the ink's viscosity (Fig. 2(a)). The TEOS precursor solution without ZrO_2 exhibits high fluidity and is entirely unsuitable for printing. With the addition of 10 wt.% ZrO_2, the viscosity increases noticeably but remains inadequate for printing. At 20 wt.% ZrO_2, the ink maintains its shape without collapsing, making it suitable for printing. Secondly, both the ink temperature (i.e., the temperature during pre-treatment in a water bath) and the temperature of the freezing platform also influence

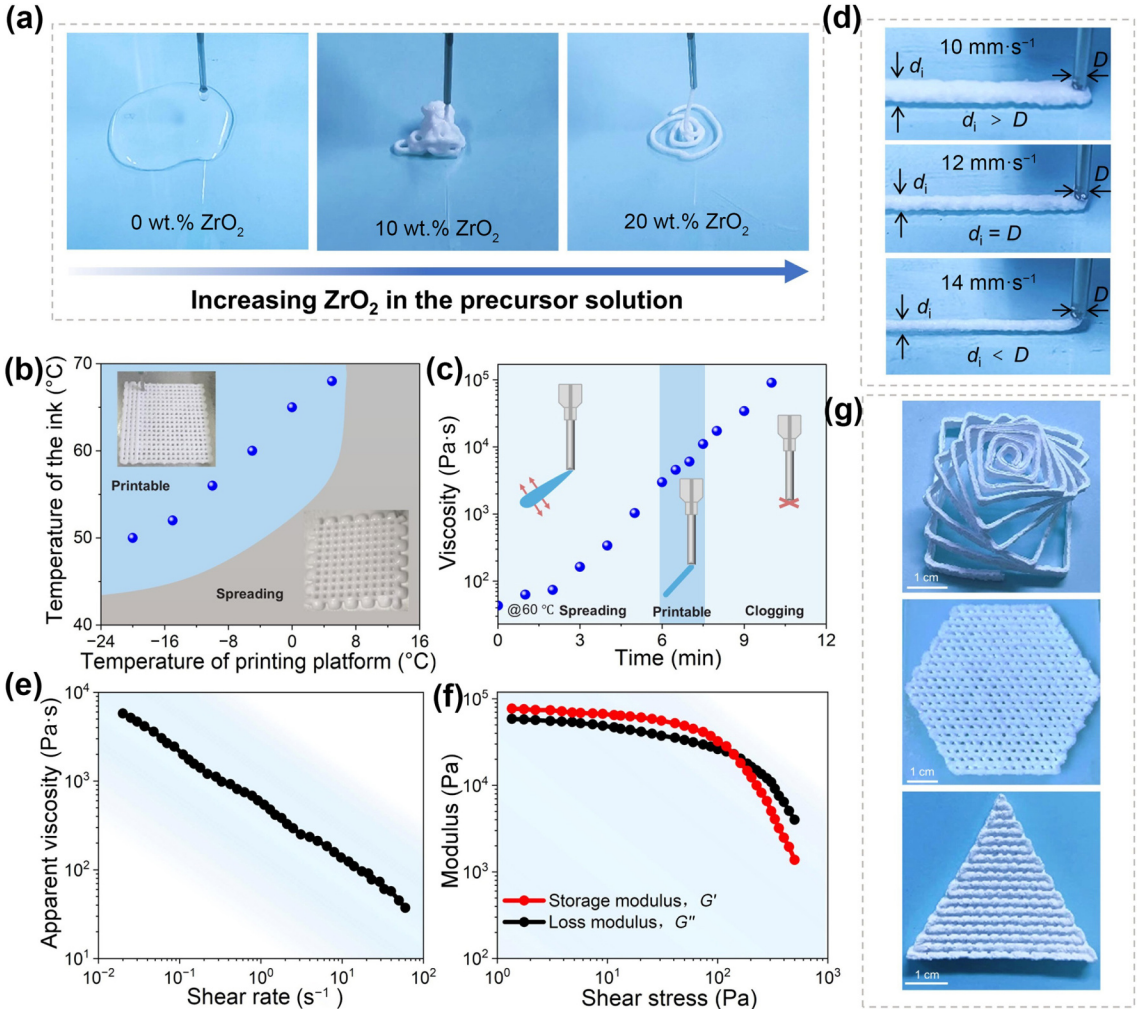

Figure 2 Control of ink viscosity and printing parameters. (a) Effect of ZrO_2 nanoparticle content on ink viscosity. (b) Influence of ink temperature and freezing platform temperature on printability. (c) Effect of ink temperature treatment duration on printability. (d) Influence of printing speed on printing path and width using a 0.84 mm nozzle. (e) Shear-thinning behavior of the ink. (f) Variation of the ink's modulus with shear stress. (g) Examples of printed structures with different geometries.

the gel morphology (Fig. 2(b)). When the ink temperature is below 45 °C, the viscosity is too low, leading to spreading during printing. When the freezing platform temperature exceeds 10 °C, the printed structure tends to collapse, especially in multi-layered printing. Only by balancing both temperatures can high-layer, structurally intact gels be successfully printed. Furthermore, the duration of the ink temperature treatment also affects viscosity (Fig. 2(c)). To ensure that the printed gel retains its structure without collapsing, a relatively high viscosity is required. However, excessively high viscosity may lead to nozzle clogging. Since the ink contains TEOS, hydrolyzing process was taken by heating the gel in a water bath (60 °C). Extensive experimentation revealed that heat treatment for less than 6 min results in ink spreading, while exceeding 8 min causes nozzle clogging. Heating at 60 °C for 7 min is appropriate for printing, at which the ink viscosity ranges roughly between 4500 and 6000 Pa·s.

Regarding printing parameters, the nozzle diameter is first optimized (Fig. S1 in the Electronic Supplementary Matreial (ESM)). A 0.41 mm nozzle can only be used in the initial printing stage, as it tends to clog due to the gradual increase in ink viscosity during printing. Although a 1.2 mm nozzle avoids clogging, the excessively wide printing path limits precise structural control. In contrast, a 0.84 mm nozzle satisfies both requirements. Furthermore, the influence of printing speed is also investigated (Fig. 2(d)). When using the 0.84 mm nozzle, a printing speed of 10 mm·s^{-1} results in a filament width (d_i) larger than the nozzle diameter (D). At 14 mm·s^{-1}, the printed filament became narrower than the nozzle diameter. A comparable width between the filament and the nozzle diameter was achieved at a printing speed of 12 mm·s^{-1}.

Rheological tests confirm the shear-thinning behavior of the ink (Fig. 2(e)). Moreover, both the storage modulus and loss modulus gradually decreased with increasing shear stress, until the storage modulus fell below the loss modulus (Fig. 2(f)). This further demonstrates the printability of the ink. Using this ink, various structures such as spirals, hexagons, and triangles could be flexibly printed (Fig. 2(g)).

3.3 Effect of printing spacing and rotation angle on thermal insulation performance

The printing spacing (x) and rotation angle (θ) significantly influence the morphology of the SiO_2/ZrO_2 aerogels (Fig. 3(a)). With x fixed at 1.6 mm, varying θ from 10° to 90° yields aerogels with distinct structural characteristics (Fig. S2 in the ESM). Computer-aided design (CAD) analysis reveals the following patterns. When θ is 90° or 60°, the SiO_2/ZrO_2 aerogels exhibit clearly interconnected pore structures, owing to their short printing cycles (Figs. S3(a) and S3(b) in the ESM). For example, the printing

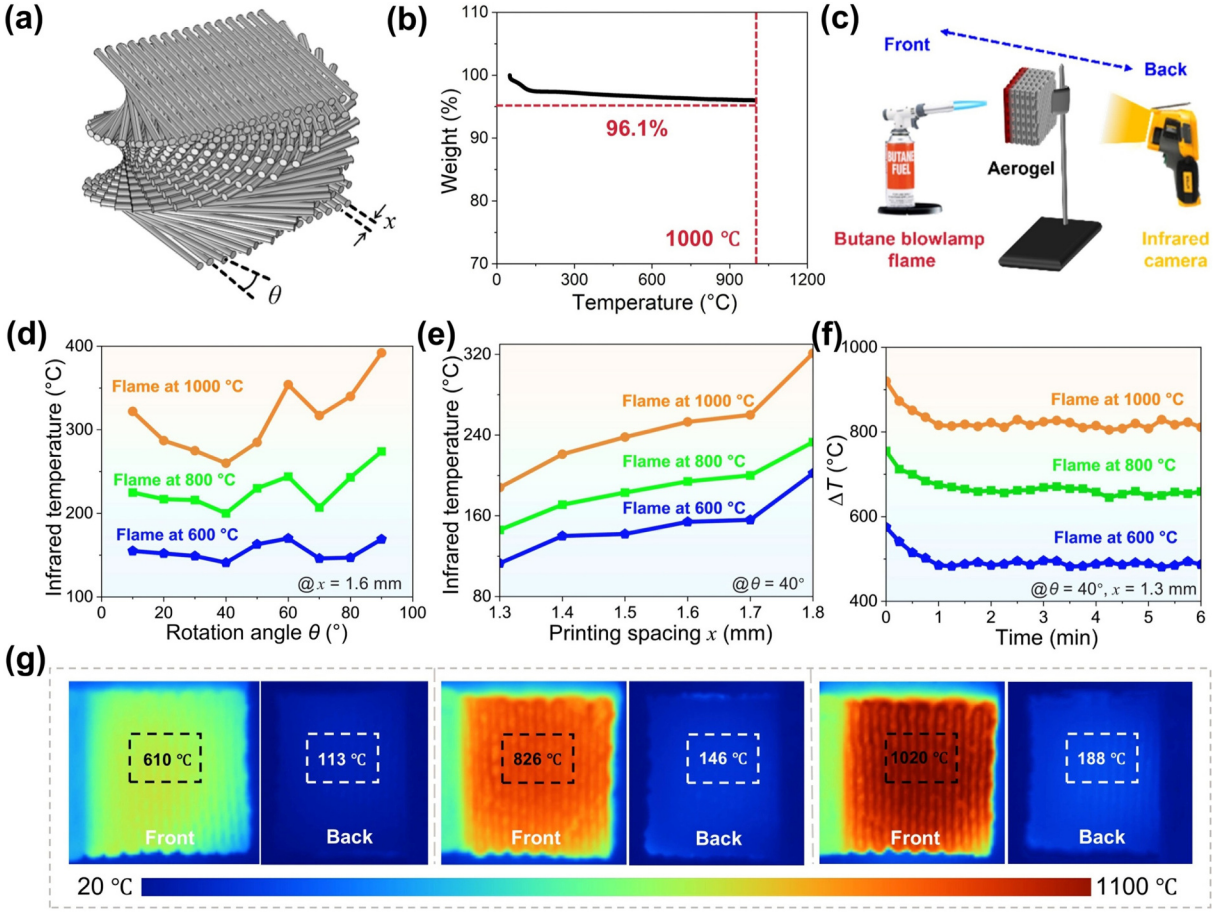

Figure 3 Effect of printing spacing and rotation angle on thermal insulation performance. (a) Printing spacing (x) and rotation angle (θ) of the SiO_2/ZrO_2 aerogels. (b) TGA of the SiO_2/ZrO_2 aerogels. (c) High-temperature flame test. The relationship between the back temperature of SiO_2/ZrO_2 aerogels (12 mm thick) and (d) the rotation angle θ (with x fixed at 1.6 mm), and (e) the printing spacing x (with θ fixed at 40°) at flame temperature of 600, 800 and 1000 °C. (f) The temperature difference (ΔT) between the flame front and back side as a function of time, and (g) the corresponding infrared images of the front and back surfaces of the SiO_2/ZrO_2 aerogels (θ = 40°, x = 1.3 and 12 mm thick).

cycle is only 2 layers for θ = 90° and 3 layers for θ = 60°. In contrast, at θ = 30°, 40°, or 80°, the aerogels develop complex small-pore structures due to longer printing cycles (Figs. S3(c)–S3(e) in the ESM). For example, the printing cycle is 9 layers for θ = 40°. However, not all angles are suitable for printing. For instance, at θ = 50° or 70°, the required printing cycles exceed the equipment's maximum layer limit (28 layers). The extremely small pores and overly complex structure cause the adjacent printing paths to attract each other and form "liquid bridges" before solidification (Fig. S4 in the ESM). This seriously affects the structure of the SiO_2/ZrO_2 aerogels (Figs. S5 and S6 in the ESM). At smaller angles such as θ = 10° or 20°, the upper surface of the aerogels exhibits varying degrees of collapse (Fig. S7 in the ESM).

Thermogravimetric analysis (TGA) of the SiO_2/ZrO_2 aerogels reveals a weight loss of less than 4% at 1000 °C, indicating excellent thermal stability (Fig. 3(b)). Thermal insulation performance is evaluated via high-temperature flame test on approximately 12 mm-thick aerogels with different θ (x = 1.6 mm) (Fig. 3(c) and Fig. S8 in the ESM). The temperature change on the back side is recorded with an infrared camera. Figure 3(d) shows the relationship between the θ and the thermal insulation performance of SiO_2/ZrO_2 aerogels (x = 1.6 mm) under flame temperatures of 600, 800, and 1000 °C. The poor thermal insulation is observed at θ = 90° or 60°. Slightly better performance is achieved at θ = 50° or 70°. The structural collapse at θ = 10° or 20° reduces insulation effectiveness. Aerogels with θ = 30°, 40°, or 80° exhibit intact structures and good thermal insulation.

The pore size of the aerogel significantly influences its thermal insulation performance. The thermal conductivity (κ) can be characterized using the following theoretical model (Eq. (1))

$$k = fk_{air} + (1-f)k_{solid} \quad (1)$$

where k_{air} and k_{solid} represent the thermal conductivity of the gas and the solid respectively, and f denotes the porosity. According to the Knudsen effect, when the pore size approaches the mean free path of gas molecules, k_{air} is significantly reduced (Eq. (2))

$$\begin{cases} k_{air} = \dfrac{k_{air0}}{1+2\dfrac{(2-\alpha)2\gamma}{\alpha(1+\gamma)}\dfrac{1}{P_r}K_n} \\ K_n = \dfrac{k_B T}{\pi\sqrt{2}d_g^2 P L_c} \end{cases} \quad (2)$$

where k_{air0} is the thermal conductivity of free air, α is a scaling coefficient, γ is the adiabatic index, P_r is the Prandtl number, K_n is the Knudsen number, k_B is the Boltzmann constant, T is temperature, P is pressure, L_c is the characteristic pore length, and d_g is the gas molecular diameter.

Therefore, when θ = 90° or 60°, the pore size of the SiO_2/ZrO_2 aerogels significantly exceeds the mean free path of gas molecules, which facilitates rapid heat transfer. This heat transfer mechanism ultimately leads to poor thermal insulation performance. At θ = 50° or 70°, the mutual attraction between uncured printing paths forms "liquid bridges", causing path fusion and blocking originally designed pores. This substantially increases solid-phase heat conduction. For θ = 10° or 20°, structural collapse on the surface of the aerogels disrupts the predefined pore architecture, significantly weakening the Knudsen effect and reducing insulation performance. In contrast, aerogels with θ = 30°, 40° or 80° avoid the issues of through-pores, "liquid bridges" and structural collapse, demonstrating improved thermal insulation. Notably, at θ = 40°, the constructed microstructure effectively elongates the heat conduction paths, suppressing thermal convection while enhancing the infrared reflection. As a result, the aerogel exhibits excellent thermal insulation performance.

Fixing θ at 40°, the high-temperature flame tests are carried out for the 12 mm thickness SiO_2/ZrO_2 aerogels with varying x values (Fig. S9 in the ESM). Figure 3(e) illustrates the relationship between the infrared temperature of the back surface and x at flame temperatures of 600, 800, and 1000 °C on the front surface of the SiO_2/ZrO_2 aerogels. As x decreases, the thermal insulation performance progressively improves. CAD analysis reveals that the average pore size of the SiO_2/ZrO_2 aerogels decreases with reduced x, thereby enhancing the Knudsen effect and improving thermal insulation (Fig. S10 in the ESM). The influence of printing thickness on the thermal insulation performance of the SiO_2/ZrO_2 aerogels is also investigated (Fig. S11 in the ESM).

Prolonged tests for the SiO_2/ZrO_2 aerogel (θ = 40° and x = 1.3 mm) were carried out under a high-temperature flame at 1000 °C for 10 min (Fig. S8(a) in the ESM). The average infrared temperature on the backside remains as low as 188 °C (Figs. 3(f) and 3(g)). Moreover, there is hardly any volume and mass change, demonstrating the long-term thermal stability of the SiO_2/ZrO_2 aerogel (Table S1 in the ESM).

To investigate the potential influence of ambient humidity on the thermal insulation performance of the SiO_2/ZrO_2 aerogels, we created a high-humidity environment (65% RH) using a humidifier. Then thermal insulation tests were then performed for the aerogels (θ = 90° and x = 1.3 mm) in both the high-humidity environment and dry atmosphere. The results show that the thermal insulation performance of the aerogel exhibited no significant difference between the dried aerogel and the high humidity-treated aerogel (Fig. S12 in the ESM).

The microstructure of the SiO_2/ZrO_2 aerogels (θ = 40°, x = 1.3 mm) are characterized by scanning electron microscopy (SEM) combined with ImageJ software analysis. The analysis shows that the aerogels contain nanoscale pores, with an average pore size of 491 nm in the cross-sectional view (Figs. 1(e) and 1(f)). The average surface pore size is approximately 516 nm, while the longitudinal section exhibits an average pore size of about 485 nm (Fig. S13 in the ESM). These results indicate that the aerogels possess uniformly distributed nanopores across different directions, demonstrating their potential for thermal insulation applications.

3.4 Arctangent-topological pore structure design for the SiO_2/ZrO_2 aerogels

Given the critical influence of pore size and distribution on the thermal insulation of aerogels, we introduce a mathematical function to segment the square pore architecture. Specifically, the arctangent function is defined as $\alpha_n = \arctan(1/n)$, where n is a non-negative integer. For a square structure, a larger n corresponds to increased partitioning multiplicity (Fig. S14(a) in the ESM). During printing, a set of parallel paths (1.3 mm) and oriented at α_n from the vertical direction are first printed, along with their perpendicular counterparts. A fourfold rotationally symmetric aerogel is then fabricated using the central cross-axis as the symmetry reference. This methodology is defined as the arctangent-topological DIW strategy. When n = 0, 1, 2 (α_n = 90°, 45°, 26.6°, respectively), SiO_2/ZrO_2 aerogels exhibit clear and intact structures, designated as Model I, Model II, and Model III (Fig. S14(b) in the ESM).

However, for $n \geq 3$, the small angles lead to structural collapse and loss of integrity, so it is no longer considered (Fig. S14(c) in the ESM). For comparison, the aerogels with $\theta = 40°$ and $x = 1.3$ mm is defined as Model IV (Fig. 4(a)). Figure 4(b) shows photographs and dimensions of these four models.

3.5 Thermal insulation and mechanical performances of the four aerogel models

Thermal insulation performance of the four aerogel models (12 mm thick) is evaluated via high-temperature flame tests (Figs. 4(c)–4(e)). Model IV demonstrates the best insulation performance, followed by Model III, then Model II, while Model I exhibits the poorest performance. The inferior insulation of Model I is attributed to its vertically aligned overlapping structure, which forms continuous high thermal conductivity channels. Model II divides the square structure via 45° diagonals, reducing pore size and improving insulation compared to Model I. Model III employs a more complex periodic unit division, resulting in more tortuous heat transfer paths and superior insulation relative to Model I and Model II. The asymmetric architecture of Model IV maximally avoids the formation of periodic thermal channels. Compared to Model III, the pore structure and distribution of Model IV provide superior reduction in thermal conduction, convection, and radiation, resulting in optimal thermal insulation performance (Figs. S10(f) and S14(b) in the ESM).

Thermal insulation simulations of the four models are conducted using COMSOL Multiphysics. A rectangular unit measuring 0.84 mm × 0.84 mm × 22.34 mm is employed as the structural element, and 256 such units are assembled according to the respective model to form the full simulation model. The overall dimensions of the simulation model closely match those of the physical samples (Fig. S15(a) in the ESM). The models are filled

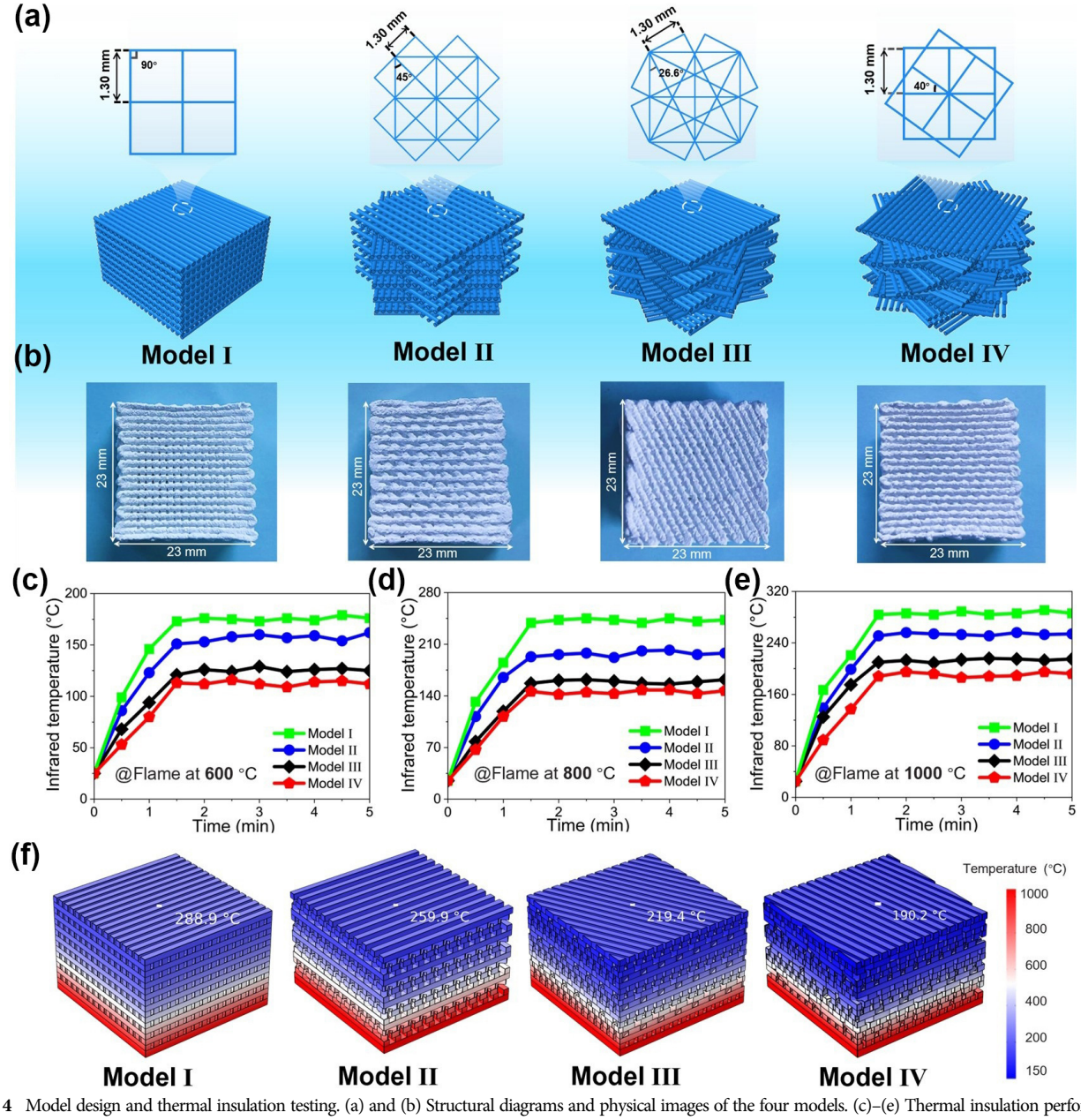

Figure 4 Model design and thermal insulation testing. (a) and (b) Structural diagrams and physical images of the four models. (c)–(e) Thermal insulation performance of the four models under flame temperatures of 600, 800, and 1000 °C. (f) COMSOL-based thermal simulation of the four models.

with a porous material, where the fluid phase is air. The density, thermal conductivity, constant pressure coefficient and porosity of the solid part are all the same as the actual material parameters (Table S2 in the ESM). A highly conductive copper plate (401 $W·m^{-1}·K^{-1}$) with dimensions of 22.34 mm × 22.34 mm × 1 mm is placed at the bottom of the model to simulate a heat source. A temperature boundary condition is applied at the bottom of the copper plate to ensure uniform heating of the model above. The ambient temperature and initial material temperature are set to 20 °C. The heat flux type is defined as convective heat flux, and a steady-state solver is used. After applying temperatures of 600, 800, and 1000 °C respectively, the simulation results show that at 1000 °C, the top surface temperatures of the four models are 288.9, 259.9, 219.4, and 190.2 °C (Fig. 4(f)). The insulation performance ranking aligns with experimental observations, and the numerical error between simulation and experiment was within 5%. Similarly, at 600 and 800 °C, the simulation results remained consistent with experimental data, with errors not exceeding 10% (Figs. S15(b) and S15(c) in the ESM).

Considering the thermal irradiation effect, heat transfer simulations are carried out for the four models under a 1000 °C heat source. The simulation is performed by adding the thermal radiation physics interface to the existing models using COMSOL Multiphysics software. The relevant parameters were configured as follows: absorption coefficient k = 100 m^{-1}, scattering coefficient σ_s = 1000 m^{-1}, and refractive index of 1.5. Other thermophysical parameters, such as porosity and thermal conductivity, remained entirely consistent with the previous setup (Table S2 in the ESM). The boundary conditions were established with the bottom copper plate as the heating source. A condition of continuous contact was assumed between the heating plate and the aerogel model. Since the aerogel itself has a high emissivity, thermal radiation from the aerogel to the surrounding environment should also be considered. The emissivity of the aerogels and the ambient temperature was set as 0.8 and 20 °C, respectively. Multiphysics coupling was performed between the radiative heat transfer and solid heat transfer interfaces. The subsequent steps, including meshing and solver settings, followed the same procedures as before and will not be reiterated here. The results are shown in Fig. S16 in the ESM. The surface temperature of the aerogel decreased in all four models. This effect is relatively similar to the thermal radiation management mechanism observed in cactus.

Subsequently, the mechanical behaviors of the four models under uniaxial compression are investigated. Compressive loads are applied either parallel or perpendicular to the thickness direction of the aerogels (Figs. 5(a) and 5(b)). The results indicate that the compressive strength is in descending order for Model I, Model III, Model II, and Model IV, respectively.

Similarly, mechanical compression simulations of the four models are conducted via COMSOL Multiphysics (Fig. 5(c) and Fig. S17 in the ESM). The modeling method and dimensions are identical to those used in the thermal insulation simulations. All models employ an elastoplastic constitutive model, with their elastic modulus, Poisson's ratio, yield strength, and other parameters provided in Table S3 in the ESM. Additionally, two platens are constructed at the top and bottom or left and right ends of the model to simulate compression parallel or perpendicular to the thickness direction of the aerogels. For compression parallel to the thickness direction, the bottom platen is fixed, and the top platen is only applied to a displacement corresponding to 10% strain along the thickness direction. For compression perpendicular to the thickness direction, the left platen is fixed, and the right platen is only applied a displacement corresponding to 10% strain in the perpendicular direction. The simulations are solved using a parametric sweep method with strain increments of 0.5%, and a steady-state solver is used.

The simulation results indicate that Model I exhibits relatively uniform stress distribution and weak stress concentration, with no significant lateral forces or bending moments, resulting in optimal compressive performance. The simulation results for Model II indicate that bending deformation of its structural units leads to pronounced stress concentration. The structure experiences an inefficient loading state, being subjected to simultaneous significant compression and bending. Consequently, only a fraction of the materials in Model II effectively contribute to load-bearing. In Model III, the inclined structural units are subjected primarily to axial compression, with bending as a secondary loading mode. The stress nephogram directly indicates that most of the material still participates in load-bearing. The simulation results for Model IV reveal highly non-uniform stress distribution, where the load is borne only by localized regions aligned with or nearly parallel to the loading direction. Thus, most of the materials do not effectively contribute to load-bearing, resulting in low stress levels and the poorest utilization of material strength.

Considering both thermal insulation and mechanical properties, Model III demonstrates high compressive strength (341.7 kPa), effective thermal insulation (33.9 $mW·m^{-1}·K^{-1}$), and a high operating temperature (1100 °C) (Fig. 5(d)). Comparing with SiC nanofiber aerogels (~ 840 kPa, 37–41 $mW·m^{-1}·K^{-1}$, 1200 °C) [30, 31], ZrO_2 composite aerogels (~ 110 kPa, 25–36 $mW·m^{-1}·K^{-1}$, 1300 °C) [32–34], Al_2O_3 composite aerogels (~ 860 kPa, 55–65 $mW·m^{-1}·K^{-1}$, 1800 °C) [35, 36] and SiO_2 composite aerogels (~ 810 kPa, 19–49 $mW·m^{-1}·K^{-1}$, 1300 °C) [37–41], the SiO_2/ZrO_2 aerogels (Model III) fabricated in this work achieve a synergistic improvement in both thermal insulation and mechanical properties (Fig. 5(e)).

3.6 Thermal insulation applications of SiO_2/ZrO_2 aerogels (Model III)

High-temperature thermal insulation aerogels exhibit broad applications. For instance, they provide critical thermal isolation for battery components during electric vehicle thermal runaway events to prevent catastrophic failures (Fig. 6(a)). They can also serve as thermal barriers for high-temperature surfaces, such as engine combustion chamber walls (Fig. 6(b)). For electric chips, the SiO_2/ZrO_2 aerogels can be used to effectively mitigate localized hotspots in chips, lessening damages to the surrounding thermally sensitive devices. As demonstrated in Figs. 6(c_1) and 6(c_2), SiO_2/ZrO_2 aerogel caps are fabricated and placed on chips, with their insulation performance compared to PI aerogel caps (Fig. S18 in the ESM). Using a PTC heater set at 242–260 °C, the localized temperature of the chip protected by the SiO_2/ZrO_2 aerogel caps is only 38.2 °C, compared to 122.7 °C for the unprotected chip. Under the same conditions, the chip with PI aerogel caps exhibits a temperature of 49.8 °C (Figs. 6(c_3) and 6(c_4)), indicating that SiO_2/ZrO_2 aerogel possesses better thermal insulation than the PI aerogel.

To simulate the thermal insulation behavior encountered in engine combustion chambers, the SiO_2/ZrO_2 aerogel is assembled around the nozzle of a high-temperature flame. After 3 min of heating, the surface temperature of the nozzle reaches 575 °C, while

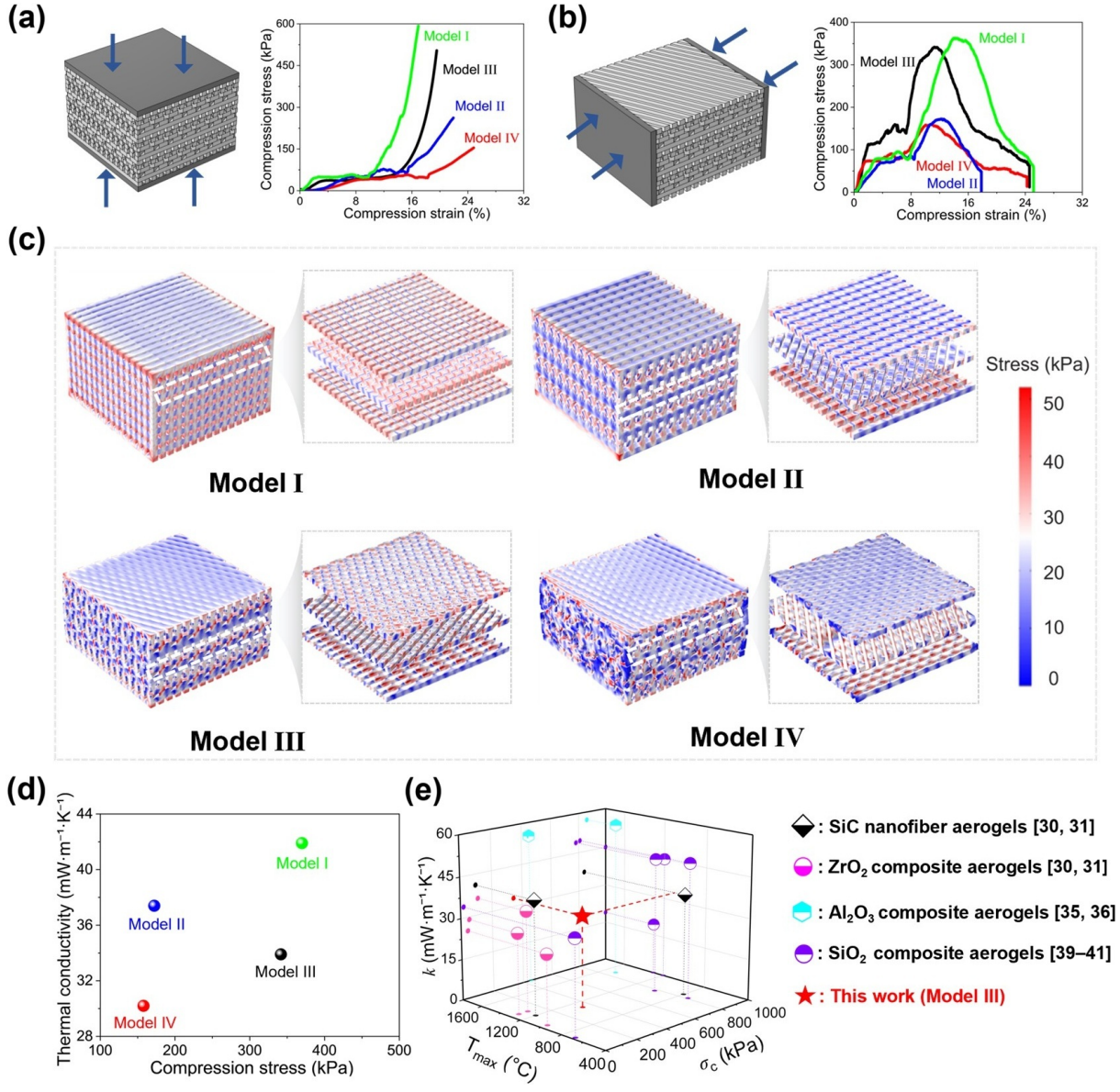

Figure 5 Mechanical performance testing and comparison of the four models. (a) and (b) Compression parallel or perpendicular to the model thickness direction and the corresponding stress-strain curves. (c) COMSOL simulation of compression parallel to the thickness direction (10% strain). (d) Comparison of mechanical compressive strength and thermal conductivity among the four models. (e) Comparison of mechanical compressive strength (σ_c), thermal conductivity (k), and maximum working temperature (T_{max}) among different aerogel materials.

the surface temperature of the SiO_2/ZrO_2 aerogels thermal shell remains only 155.6 ℃, demonstrating marked thermal insulation effectiveness (Fig. 6(d)).

4 Conclusions

Inspired by heat-tolerant spiral ridges of desert cactus, the SiO_2/ZrO_2 aerogels with controllable spiral macrostructures are designed. Via modulation of the rheology of the precursor ink, the SiO_2/ZrO_2 aerogels were fabricated combining the freezing-assisted DIW and freeze-drying. The effects of the rotation angle θ and printing spacing x on the thermal insulation performance of SiO_2/ZrO_2 aerogels are systematically investigated. The SiO_2/ZrO_2 aerogels (θ = 40°, x = 1.3 mm) possess excellent thermal insulation performance (30.2 $mW·m^{-1}·K^{-1}$), and mechanical behavior (a compressive strength of 159.3 kPa and a fracture strain of 24.2%). To simultaneously enhance thermal and mechanical properties, a printing strategy based on a quadruple rotationally symmetric structure defined by the arctangent function α_n = arctan(1/n) is proposed. At α_n = 26.6° (n = 2), the SiO_2/ZrO_2 aerogels maintain excellent thermal insulation performance (33.9 $mW·m^{-1}·K^{-1}$) while achieving a notable improvement in compressive strength, reaching 341.7 kPa, with a fracture strain of 24.6%. Compared with existing high-temperature resistant aerogels reported in the literature, this SiO_2/ZrO_2 aerogels demonstrate a remarkable balance of both excellent thermal insulation and mechanical properties. Finite element simulations of the thermal insulation and compressive mechanical properties of the SiO_2/ZrO_2 aerogels are conducted using COMSOL Multiphysics, showing good consistency with experimental results. The application tests on the chip demonstrate that the SiO_2/ZrO_2 aerogels can effectively protect electronic devices upon overheating surrounding. The protection of the pipeline near

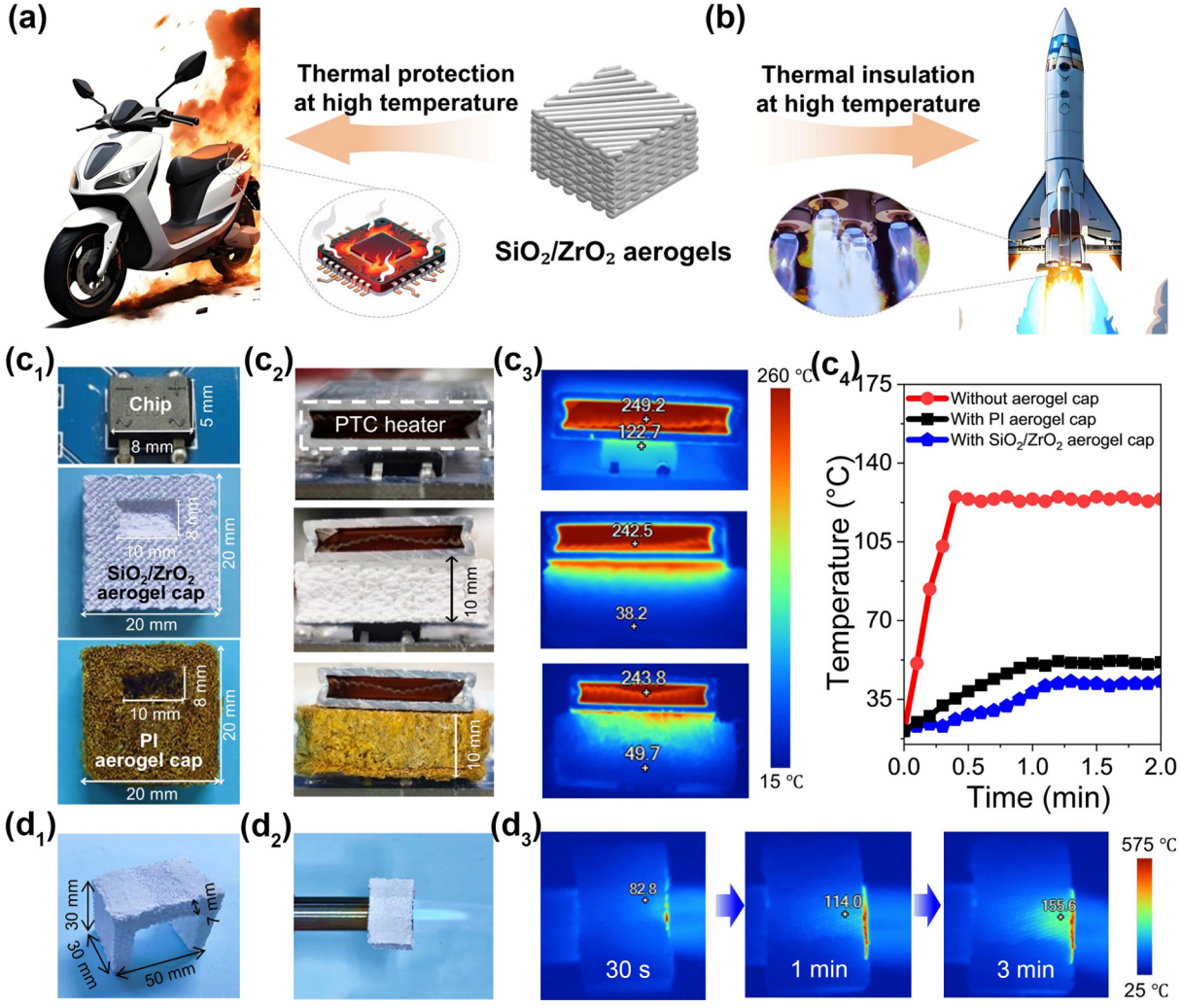

Figure 6 Thermal insulation applications of SiO_2/ZrO_2 aerogels (Model III). (a) and (b) Potential application scenarios of SiO_2/ZrO_2 aerogels. Physical images (c_1) and (c_2), infrared images (c_3), and surface temperature profiles over time (c_4) of a bare chip, a chip with SiO_2/ZrO_2 aerogel caps or PI aerogel caps under PTC heating. (d_1) and (d_2) Printed assembled SiO_2/ZrO_2 aerogel insulation shell mounted near the flame nozzle. (d_3) Variation of surface temperature on the insulation shell.

a flame nozzle further confirms their thermal insulation capability for engine combustion chambers or throats. This work offers a feasible strategy for designing aerogels with integrated long-term thermal stability and mechanical properties.

Electronic Supplementary Material: Supplementary material (Figs. S1–S12: effect of printing parameters—printing spacing, rotation angle and thickness—on thermal insulation performance of the SiO_2/ZrO_2 aerogels; Fig. S13: SEM images of the SiO_2/ZrO_2 aerogels surface and longitudinal section; Figs. S14–S17: COMSOL-based thermal simulations and mechanical compression simulations of the four models; Fig. S18: preparation of PI aerogels; and Tables S1–S3: simulations of COMSOL-based heat transfer modeling and mechanical compression modeling) is available in the online version of this article at https://doi.org/10.26599/NR.2026.94908587.

Data availability

All data needed to support the conclusions in the paper are presented in the manuscript and the Electronic Supplementary Material. Additional data related to this paper may be requested from the corresponding author upon request.

Acknowledgements

All the authors are grateful for the financial support from the National Natural Science Foundation of China (No. 12272201).

Declaration of competing interest

All the contributing authors report no conflict of interest in this work.

Author contribution statement

H. K. L. and F. F. conceived the idea. H. K. L. was the first author that performed experiments, conducted COMSOL-based simulations, and wrote the manuscript. H. K. L., W. L. L., B. C. L., X. S. S., and F. F. analyzed the data. F. F., K. Z., and X. D. H. provided some suggestions on this work. F. F. supervised and guided the project. All authors discussed the results and contributed to the manuscript.

Use of AI statement

None.

References

[1] Chang, X. Y.; Yang, Y. F.; Cheng, X. T.; Yin, X.; Yu, J. Y.; Liu, Y. T.; Ding, B. Multiphase symbiotic engineered elastic ceramic-carbon aerogels with advanced thermal protection in extreme oxidative environments. *Adv. Mater.* **2024**, *36*, 2406055.

[2] Guo, J. R.; Fu, S. B.; Deng, Y. P.; Xu, X.; Laima, S.; Liu, D. Z.; Zhang, P. Y.; Zhou, J.; Zhao, H.; Yu, H. X. et al. Hypocrystalline ceramic aerogels for thermal insulation at extreme conditions. *Nature* **2022**, *606*, 909–916.

[3] Wang, H. X.; Cheng, L. D.; Yu, J. Y.; Si, Y.; Ding, B. Biomimetic Bouligand chiral fibers array enables strong and superelastic ceramic aerogels. *Nat. Commun.* **2024**, *15*, 336.

[4] Zhao, S. Y.; Siqueira, G.; Drdova, S.; Norris, D.; Ubert, C.; Bonnin, A.; Galmarini, S.; Ganobjak, M.; Pan, Z. Y.; Brunner, S. et al. Additive manufacturing of silica aerogels. *Nature* **2020**, *584*, 387–392.

[5] Niu, Z. Q.; Qu, F. J.; Chen, F.; Ma, X. Y.; Chen, B. X.; Wang, L. Y.; Xu, M.; Wang, S. M.; Jin, L.; Zhang, C. S. et al. Multifunctional integrated organic-inorganic-metal hybrid aerogel for excellent thermal insulation and electromagnetic shielding performance. *Nano-Micro Lett.* **2024**, *16*, 200.

[6] Zhang, Z. X.; Deng, Y. R.; Lun, Z.; Zhang, X.; Yan, M. Y.; He, P.; Li, C. H.; Pan, Y. L. Mechanically strong and tailorable polyimide aerogels prepared with novel silicone polymer crosslinkers. *Gels* **2022**, *8*, 57.

[7] Zhang, E. S.; Zhang, W. L.; Lv, T.; Li, J.; Dai, J. X.; Zhang, F.; Zhao, Y. M.; Yang, J. Y.; Li, W. J.; Zhang, H. Insulating and robust ceramic nanorod aerogels with high-temperature resistance over 1400 °C. *ACS Appl. Mater. Interfaces* **2021**, *13*, 20548–20558.

[8] Wang, S. M.; Wang, H.; Wang, W. G.; Li, H.; Yang, J. J.; Li, D. D. Fabrication of PI/SiO_2 composite aerogels via an *in-situ* co-gel strategy for integrated thermal and acoustic insulation. *J. Mater. Sci. Technol.* **2026**, *245*, 208–220.

[9] Zhan, H. J.; Wu, K. J.; Hu, Y. L.; Liu, J. W.; Li, H.; Guo, X.; Xu, J.; Yang, Y.; Yu, Z. L.; Gao, H. L. et al. Biomimetic carbon tube aerogel enables super-elasticity and thermal insulation. *Chem* **2019**, *5*, 1871–1882.

[10] Wang, J.; Shan, X. M.; Hu, P. Y.; Zhang, C. J.; Yuan, D. S.; Hu, X. Y.; Wang, J. Bioinspired multilayer structures for energy-free passive heating and thermal regulation in cold environments. *ACS Appl. Mater. Interfaces* **2022**, *14*, 46569–46580.

[11] Wu, M. R.; Shao, Z. Y.; Zhao, N. F.; Zhang, R. Z.; Yuan, G. D.; Tian, L. L.; Zhang, Z. B.; Gao, W. W.; Bai, H. Biomimetic, knittable aerogel fiber for thermal insulation textile. *Science* **2023**, *382*, 1379–1383.

[12] Zhuge, Y. N.; Liu, F. J. Recent progress of bionic hierarchical structure in the field of thermal insulation protection. *J. Bionic Eng.* **2024**, *21*, 1–18.

[13] Zheng, J. J.; Li, Z.; Wei, N.; Gao, M. Y.; Bai, T. X.; Zhang, J. Y.; Zhang, X. H.; Zhu, M. F.; Cheng, Y. H. Roll-to-roll twisted aerogel yarns with reinforced structure and low thermal conductivity. *Adv. Mater.* **2025**, *37*, 2507289.

[14] Zhang, Z. Q.; Cui, B. Y.; Sun, Y. N.; Shan, J.; Li, S.; Hao, S.; Shan, W. D.; Wang, W. H.; Song, Y. M.; Fang, Y. Q. et al. Biomimetic gradual helical structure for enhancing the strength and toughness of fiber-reinforced composites. *Adv. Mater.* **2025**, *37*, 2501166.

[15] Wen, S. M.; Gao, W. T.; Zhang, S. C.; Pang, J.; Cui, C.; Gao, H. L.; Zheng, Z. J.; Chen, S. M.; Yu, S. H. Gradient double-twisted Bouligand structural design for high impact resistance over a wide range of loading velocities. *Sci. Adv.* **2025**, *11*, eadv2169.

[16] Zhang, X.; Zhao, X. Y.; Xue, T. T.; Yang, F.; Fan, W.; Liu, T. X. Bidirectional anisotropic polyimide/bacterial cellulose aerogels by freeze-drying for super-thermal insulation. *Chem. Eng. J.* **2020**, *385*, 123963.

[17] Zhu, J. H.; Zhou, H.; Wang, C.; Zhou, L.; Yuan, S. Q.; Zhang, W. H. A review of topology optimization for additive manufacturing: Status and challenges. *Chin. J. Aeronaut.* **2021**, *34*, 91–110.

[18] Saadi, M. A. S. R.; Maguire, A.; Pottackal, N. T.; Thakur, M. S. H.; Ikram, M. M.; Hart, A. J.; Ajayan, P. M.; Rahman, M. M. Direct ink writing: A 3D printing technology for diverse materials. *Adv. Mater.* **2022**, *34*, 2108855.

[19] Yang, J. M.; Lu, J. L.; Han, D. X.; Zhou, B.; Du, A. Direct ink writing of aerogels: Fundamentals, strategies, applications, and perspectives. *Prog. Mater. Sci.* **2025**, *152*, 101462.

[20] Wang, S.; Ding, R. D.; Liang, G. Q.; Zhang, W.; Yang, F. J.; Tian, Y. C.; Yu, J. Y.; Zhang, S. C.; Ding, B. Direct synthesis of polyimide curly nanofibrous aerogels for high-performance thermal insulation under extreme temperature. *Adv. Mater.* **2024**, *36*, 2313444.

[21] Xue, T. T.; Yuan, S. J.; Yang, Y.; Wan, X.; Yang, Y. J.; Mu, X. S.; Zhang, L. S.; Zhang, C.; Fan, W.; Liu, T. X. Freezing-assisted direct ink writing of customized polyimide aerogels with controllable micro- and macro- structures for thermal insulation. *Adv. Funct. Mater.* **2025**, *35*, 2417734.

[22] Miao, M. L.; Yin, J. N.; Mao, Z. Y.; Chen, Y. H.; Lu, J. 3D-printed mullite-reinforced SiC-based aerogel composites. *Small* **2024**, *20*, 2401742.

[23] Cui, C.; Zhuang, Z. Y.; Gao, H. L.; Pang, J.; Pan, X. F.; Yu, S. H. 3D printing of ultrahigh filler content composites enabled by granular hydrogels. *Adv. Mater.* **2025**, *37*, 2500782.

[24] Cheng, Q. Q.; Sheng, Z. Z.; Wang, Y. F.; Lyu, J.; Zhang, X. T. General suspended printing strategy toward programmatically spatial kevlar aerogels. *ACS Nano* **2022**, *16*, 4905–4916.

[25] Guo, P. F.; Su, L.; Peng, K.; Lu, D.; Xu, L.; Li, M. Z.; Wang, H. J. Additive manufacturing of resilient SiC nanowire aerogels. *ACS Nano* **2022**, *16*, 6625–6633.

[26] Feng, C. A.; Yu, S. S. 3D printing of thermal insulating polyimide/cellulose nanocrystal composite aerogels with low dimensional shrinkage. *Polymers* **2021**, *13*, 3614.

[27] Wang, L. K.; Feng, J. Z.; Luo, Y.; Jiang, Y. G.; Zhang, G. J.; Feng, J. Versatile thermal-solidifying direct-write assembly towards heat-resistant 3D-printed ceramic aerogels for thermal insulation. *Small Methods* **2022**, *6*, 2200045.

[28] Wang, L. K.; Feng, J. Z.; Luo, Y.; Zhou, Z. H.; Jiang, Y. G.; Luo, X. F.; Xu, L.; Li, L. J.; Feng, J. Three-dimensional-printed silica aerogels for thermal insulation by directly writing temperature-induced solidifiable inks. *ACS Appl. Mater. Interfaces* **2021**, *13*, 40964–40975.

[29] Rau, D. A.; Williams, C. B.; Bortner, M. J. Rheology and printability: A survey of critical relationships for direct ink write materials design. *Prog. Mater. Sci.* **2023**, *140*, 101188.

[30] Hou, X. B.; Li, Y.; Luo, X. G.; Zhang, R. B. SiC whiskers-reinforced polyimide aerogel composites with robust compressive properties and efficient thermal insulation performance. *J. Appl. Polym. Sci.* **2021**, *138*, 49892.

[31] Su, L.; Jia, S. H.; Ren, J. Q.; Lu, X. F.; Guo, S. W.; Guo, P. F.; Cai, Z. X.; Lu, D.; Niu, M.; Zhuang, L. et al. Strong yet flexible ceramic aerogel. *Nat. Commun.* **2023**, *14*, 7057.

[32] Wu, C.; Jiang, J. F.; Dong, C. Y.; Zhao, L. M.; Liu, J. B.; Liu, C.; Deng, H. L.; Hui, K. N.; Pang, H.; Yan, Y. et al. Remarkably enhance the stealth/resistance/mechanical properties of silica-zirconia ceramic aerogel by phase transitions and interface evolution. *Adv. Funct. Mater.* **2025**, *35*, 2505742.

[33] Dang, S. X.; Guo, J. R.; Deng, Y. P.; Yu, H. X.; Zhao, H.; Wang, D. L.; Zhao, Y. D.; Song, C. Y.; Chen, J. L.; Ma, M. L. et al. Highly-buckled nanofibrous ceramic aerogels with ultra-large stretchability and tensile-insensitive thermal insulation. *Adv. Mater.* **2025**, *37*, 2415159.

[34] Zhang, X. X.; Wang, F.; Dou, L.; Cheng, X. T.; Si, Y.; Yu, J. Y.;

Ding, B. Ultrastrong, superelastic, and lamellar multiarch structured ZrO_2–Al_2O_3 nanofibrous aerogels with high-temperature resistance over 1300 °C. *ACS Nano* **2020**, *14*, 15616–15625.

[35] Peng, F.; Jiang, Y. G.; Feng, J.; Liu, F. Q.; Feng, J. Z.; Li, L. J. Novel silica-modified boehmite aerogels and fiber-reinforced insulation composites with ultra-high thermal stability and low thermal conductivity. *J. Eur. Ceram. Soc.* **2022**, *42*, 6684–6702.

[36] Liu, F. Q.; Jiang, Y. G.; Peng, F.; Feng, J. Z.; Li, L. J.; Feng, J. Fiber-reinforced alumina-carbon core-shell aerogel composite with heat-induced gradient structure for thermal protection up to 1800 °C. *Chem. Eng. J.* **2023**, *461*, 141721.

[37] Xu, L.; Jiang, Y. G.; Feng, J. Z.; Feng, J.; Yue, C. W. Infrared-opacified Al_2O_3–SiO_2 aerogel composites reinforced by SiC-coated mullite fibers for thermal insulations. *Ceram. Int.* **2015**, *41*, 437–442.

[38] Jiang, D. P.; Qin, J.; Zhou, X. F.; Li, Q. L.; Yi, D. Q.; Wang, B. Improvement of thermal insulation and compressive performance of Al_2O_3–SiO_2 aerogel by doping carbon nanotubes. *Ceram. Int.* **2022**, *48*, 16290–16299.

[39] Liu, R. L.; Dong, X.; Xie, S. T.; Jia, T.; Xue, Y. J.; Liu, J. C.; Jing, W.; Guo, A. R. Ultralight, thermal insulating, and high-temperature-resistant mullite-based nanofibrous aerogels. *Chem. Eng. J.* **2019**, *360*, 464–472.

[40] Liu, M.; Kong, Y.; Tang, J.; Zhang, B. Q.; Shen, X. D. Structure and performance evolutions with temperature, stress, and thermal-force coupling of the silica aerogel composite for suppressing thermal runaway propagation of LIBs. *Compos. Part A: Appl. Sci. Manuf.* **2025**, *190*, 108692.

[41] Kong, Y.; Tang, F. C.; Tan, Z. T.; Shen, X. D. Bifunctionalized hybrid silica aerogels for stable low-concentration CO_2 capture and thermal insulation under humid and high-temperature conditions. *Green Chem. Eng*. **2026**, *7*, 428–435.